Franson interferometer for characterizing highly non-degenerate correlated biphoton sources

A. J. Fallon,* E. J. Katz, I. R. Nemitz, and J. D. Lekki

NASA John H. Glenn Research Center, Cleveland, OH 44135, USA
*adam.fallon@nasa.gov

Abstract: We report the demonstration of a Franson interferometer for a highly non-degenerate time-energy entangled biphoton source. A Franson interferometer realizes a Bell test for time-energy entanglement and can thus be used to verify entanglement distribution in quantum networks and security in quantum key distribution. The highly non-degenerate source has signal and idler photons at 810 nm and 1550 nm, respectively, making this source a potential interconnect between free-space and fiber optic quantum networks. We observe a single channel visibility of $\mathcal{V} = 0.992(6)$ with an average visibility over the four output channels of $\mathcal{V} = 0.984(3)$. These visibilities overcome the visibility threshold necessary in closing the postselection loophole in the Franson interferometer Bell test.

1. Introduction

Long-distance links between quantum networks have several envisioned applications, including distributed quantum computing, quantum sensor networks, and enhanced communication security through methods such as quantum key distribution (QKD) [1–3]. The development of free-space quantum communications links comprising airborne or spaceborne assets are critical in the near term to enable these long-distance quantum links between widely separated assets, such as any of the regional quantum networks currently under development [4, 5]. Using direct connections over terrestrial fiber optic networks, these interconnections are only feasible up to several hundred kilometers at most before losses become too high [6]. On the other hand, free-space quantum links have been demonstrated beyond 1000 km [7, 8].

If two regional terrestrial networks are connected via an air- or spaceborne link, it is possible the terrestrial networks and free-space links may utilize different wavelengths. It is likely that one would choose the terrestrial network to fall within the telecommunications bands near 1300 nm or 1550 nm, while in the free-space links there would be more freedom of wavelength choice. Reasons for a specific wavelength selection could include either the targeting of transparency bands in the atmosphere [9] or taking advantage of smaller divergence angles at shorter wavelengths, either of which can improve photon-starved space-ground link margins depending on full system considerations [10, 11], or being resonant with specific atomic transitions to employ quantum memory within the greater quantum network [4, 5, 12–17]. Thus, a source that generates highly non-degenerate photons is envisioned to serve as a quantum interconnect between varied networks comprising space, airborne, and terrestrial assets, or, more generally, any two networks of differing wavelengths. Pair non-degeneracies spanning nearly four octaves have been demonstrated [18], enabling wider choice of network architectures. Furthermore, non-degenerate biphoton pairs have been at the center of recent quantum communications protocol demonstrations featuring time-bin multiplexing [19], multi-user scenarios [20], and long-distance teleportation involving a solid-state qubit [16].

Quantum metrologies for free space quantum communication sub-components and systems are needed to support the development and monitoring of quantum networks. These metrologies are used in quantifying non-classical properties and are used in trade-studies for verification and validation of performance applicability to quantum network architectures of interest. Franson interferometry, one such metrology, realizes a Bell test for quantum correlations in time-energy or time-bin degrees of freedom [21], and has been shown to demonstrate fundamental non-classical

outcomes in a wide range of biphoton sources, including those based on spontaneous parametric down-conversion (SPDC) [18, 22, 23], quantum dots [24], and spontaneous four-wave mixing [25, 26]. Furthermore, Franson interferometers have been implemented partially [25, 27–29] and completely [30–32] in fiber optics and with a solid-state quantum memory comprising one arm of the interferometer [15, 17].

Franson interferometers quantify the fidelity of time-energy or time-bin entanglement in quantum networks or their proximate components [33], as well as the security of time–energy entanglement-based QKD protocols [31] (the latter can also be addressed via another method based on dispersive optics [34–37]). In both applications, entangled photons are distributed to separate receivers – Alice and Bob. The resulting measurement visibility, $\mathcal{V}$, is related to the fidelity [23] or the quantum bit error rate [38] maintained through the link. Interferometric visibilities exceeding 94.6% for Bell tests (in certain configurations described below) [39] and 97% in QKD applications [31, 40] are typically necessary. Any reduction in visibility can be indicative of either noise or the presence of an eavesdropper in the quantum channel; hence, greater measurement precision generally allows for higher verifiable fidelity and an increased secure key rate.

Here we present the results of a Franson interferometer measurement demonstrating high visibility non-classical correlations. Most Franson interferometer implementations to date have been with degenerate or near degenerate sources [19, 22–25, 31]. The limited number looking at highly non-degenerate sources have reported low visibilities, making them unsuitable for verifying QKD performance or overcoming key Bell test loopholes [13–16, 32, 41]. The presented iteration is optimized for use with a highly non-degenerate correlated biphoton source operating at 810 nm and 1550 nm, making it relevant for nodes that interconnect fiber optic and free space network links.

2. Methods

2.1. Theory

The general setup from Franson's original proposal [21] is composed of two symmetrical, unbalanced Mach-Zehnder interferometer (MZI) measurement stations, with no particular requirement on photon degeneracy or non-degeneracy. Prior to measurement, pairs of continuously generated time-energy entangled photons are emitted and spatially separated from one another, allowing each photon from a pair to travel into an independent interferometer. For highly non-degenerate sources, such as that used here, the two interferometers are each optimized for a specific wavelength to improve performance and are therefore not interchangeable. We will henceforth refer to the 810 nm and 1550 nm photon measurement stations as Alice and Bob, respectively.

The general experimental layout is depicted in Fig. 1. The interferometer arms have different lengths, L, with subscripts denoting the short (s) and long (ℓ) paths. The path length difference between the arms, $\Delta L = L_\ell - L_s$, nominally the same in both Alice and Bob, has a few conditions. This distance must be shorter than the pump laser coherence length but longer than the coherence length of either of the down-converted photons. Furthermore, the path length differences between the two interferometers must be shorter than the two-photon coherence length. These requirements ensure that the photons do not exhibit first order interference, which would manifest in the singles counts, N_s. Rather, the interference occurs in the rate of coincident detections, C, between the biphoton pairs after passing through their respective MZI. The short and long paths lead to different coincident detection times from the four possible combinations of paths, ss, $s\ell$, ℓs, and $\ell\ell$. Of these, based on their times-of-arrival, $s\ell$ and ℓs are distinguishable, while ss and $\ell\ell$ are indistinguishable. The coincidences in the latter interfere, exhibiting the characteristic non-classical effect of the Franson interferometer. The former do not interfere and their lack of contribution to the Bell test leads to the necessity of introducing non-local postselection, which

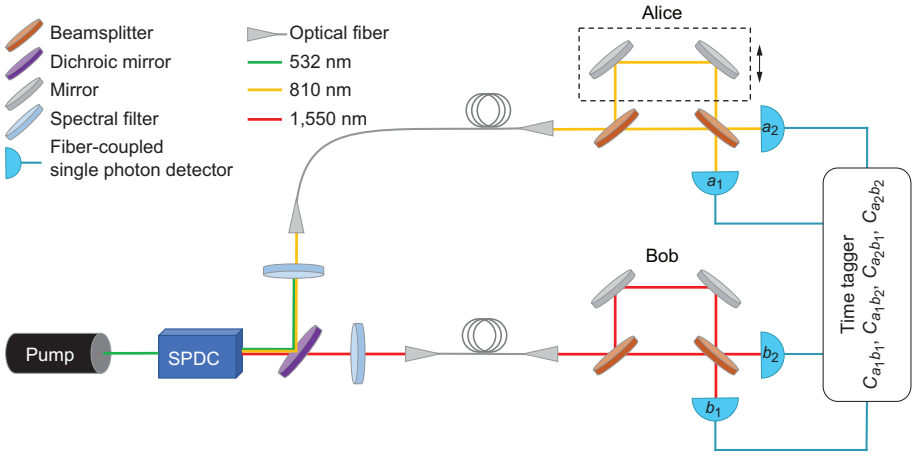

Fig. 1. Schematic of the Franson system in combination with a highly non-degenerate SPDC source. The system contains two symmetrical, unbalanced Mach-Zehnder interferometers, one for each photon wavelength, and a time tagger for photon correlation. The path length difference of Alice's interferometer is varied by moving a translation stage holding the two mirrors (dashed box).

opens the postselection loophole (PSL) [39, 42, 43].

The ss and $\ell\ell$ interference is observable in any of the four distinct coincidence rates between the detectors at Alice (a_1 and a_2) and Bob (b_1 and b_2). The interferometric phase, $\Delta\phi = (\omega_a \Delta L_a)/c + (\omega_b \Delta L_b)/c$, of the coincident detection depends on the optical frequencies of the down-converted photons, ω_i, the path length differences, ΔL_i, and the speed of light, c. The subscripts a and b denote the photons sent to Alice and Bob, respectively, as well as their local phase settings. We can vary the phase difference via changes in long path lengths of either Alice or Bob. The normalized coincidence rates for the four output channels follow the form [23]

$$C_{a_i,b_j}(\Delta\phi) = \frac{1}{4}\left(1 + (-1)^{\delta_{ij}} \mathcal{V} \cos\Delta\phi\right), \tag{1}$$

for the detectors $i, j = 1, 2$ at Alice and Bob, with an overall average visibility, $\mathcal{V}$, and the Kronecker delta, δ_{ij}.

As mentioned above, non-local postselection of the central ss and $\ell\ell$ coincidences opens the PSL. Closing this loophole is an experimentally difficult-to-overcome shortcoming of the original Franson setup, and, furthermore, it is an exploitable loophole that can undermine determination of network security using Bell tests [44]. Methods for closing this loophole include modifications to the source and/or interferometer design through the use of hyperentangled states [45], time-bin entanglement with fast switching mirrors [46, 47], or a hugging interferometer layout [23, 48]. Another approach requires the use of chained Bell inequalities [39, 49, 50], which work, in essence, by requiring more measurement settings, be it polarization projections or, as in this case, phases of the interferometers. The increase in measurements, in turn, places higher burdens on either local realism or an eavesdropper [49], depending on the desired interpretation of the test outcome. Within Franson interferometry, the ability to overcome the PSL comes at a cost, i.e., a higher visibility threshold requirement of the form [39]

$$\mathcal{V}_N = \frac{2N-1}{2N\cos\frac{\pi}{2N}}, \tag{2}$$

where N is the number of terms in the chained Bell inequality. Eqn. 2 minimizes at $N = 5$ for a

visibility threshold of $\mathcal{V}_N \approx 0.9463$ [39].

Even with this easing of visibility requirements from the worst case scenario, this violation threshold is still a significantly higher and more experimentally difficult requirement than in the more commonly known Clauser, Horne, Shimony, and Holt (CHSH) inequality, derived for a polarization Bell test, which has a visibility threshold of $\mathcal{V}_{\mathrm{CHSH}} = \frac{2}{\sqrt{2}} \approx 0.7071$ [51]. The source under test in this work is not amenable with the PSL closing modifications to either the source or interferometer due to the high non-degeneracy of the biphoton pair. This leaves the experimentally challenging visibility threshold of the chained Bell inequality method as the primary solution. The design considerations outlined in the next section enable realization of high visibility measurements.

2.2. Experimental setup

Quantum correlations are generated among a biphoton state using SPDC in a type II quasi-phase-matched periodically poled potassium titanyl phosphate (PPKTP) waveguide [52]. The process utilizes a 532 nm pump photon, which is down-converted into highly non-degenerate 810 nm and 1550 nm daughter photons. The daughter photons are then sent to Alice and Bob, respectively. The continuous wave pump laser has a coherence length > 100 m and an average power of 0.5 mW, generating approximately 10^5 detected correlated pairs per second. The waveguide source has a fiber-coupled input and free-space output. The pump light and down-converted photons exit the source colinearly and are quasi-collimated using a lens in the common beam path. Free-space sorting optics are then used to remove the remaining pump light, separate the down-converted photons, and route them into their respective single-mode optical fibers. These fibers distribute the photons to the Franson interferometer where they are coupled back into free-space. Also included within the sorting optics are interference bandpass filters with bandwidths of approximately 3 nm and 1.8 nm full width at half maximum (FWHM) for the 810 nm and 1550 nm photons, respectively, to remove unwanted spectral features from the source, at the cost of a reduced coincidence rate.

The path length differences, $\Delta L \approx 110$ mm, of the two MZIs are equalized by coarsely varying the long path of Alice over several millimeters and taking interference measurements at multiple offsets. This data is shown in Fig. 2, where the average visibility has a Gaussian profile. The 2.1 ps FWHM two-photon coincidence time is consistent with the ~1.6 ps FWHM temporal widths of the individual photons (estimated based on 1.2 nm and 2.0 nm FWHM spectroscopic measurements of the 810 nm and 1550 nm photons, respectively, taken separately with a monochromator). The detectors are composed of single-mode optical fibers connected to commercially available superconducting nanowire single photon detectors (SNSPDs). Two sets of SNSPDs are used, each having a different coating designed for increased absorption near 810 nm and 1550 nm, respectively. Their quantum efficiencies exceed 80% and 90%, jitters are 35 ps and 50 ps FWHM, and dark counts are < 100 s^{-1} and ~1000 s^{-1}. The pump laser is in the low power CW regime; therefore, higher order multi-pair emissions from the source are not significant. Together, these contribute to the high achievable visibilities reported below.

Total system detection efficiencies, measured via the Klyshko method [53], average 0.7% at 810 nm and 4.2% at 1550 nm. These efficiencies can be increased through improved mode matching between the waveguide and the single mode optical fibers, where in principle, the collection efficiency can approach unity; demonstrations exceeding 80% have been reported elsewhere [30]. Improvements within the Franson interferometer are also possible, as transmission was measured to be < 25%. Electrical outputs from the detectors are sent to a time tagger with 19 ps FWHM jitter and 1 ps resolution for coincidence detection. Local phase settings are set by changing the long path of the Alice measurement station using a translation stage adjusted via a closed-loop piezoelectric actuator with a built-in strain gauge. The actuator is capable of displacements of up to 40 μm with a 10 nm strain gauge readout resolution. The total change in

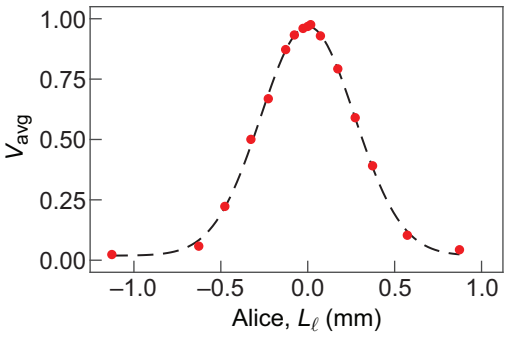

Fig. 2. Coarse alignment data. Interference visibility measurements are taken as Alice's long path is varied over several millimeters. The data are fit to a Gaussian, and a FWHM of 0.63 mm is found, corresponding to a two-photon coincidence time of 2.1 ps.

Alice's path length difference, ΔL_a, is twice the piezo's displacement. We translate in increments of ~12 nm (~0.2 radians at 810 nm) over approximately three full interference fringes. Varying Alice's path length difference while leaving Bob's fixed in this manner can reduce maximum visibility (see Fig. 2), but over the length scales used here (~1.2 μm), this effect is negligible at $< 10^{-5}$.

The interferometric visibility measurements comprise coincidence measurements taken over a 5 s integration time at 100 distinct phase settings, $\Delta\phi$. The total number of coincidences at each setting is determined by summing the counts detected within a 400 ps window around the central ss and $\ell\ell$ coincidence peaks. This is done for each of the four coincidence channels between the detectors at Alice and Bob. Example data showing $\Delta\phi \approx 0$ and π are given in Fig. 3. The four channels have individual coincidence detection rates of between 400 s^{-1} and 700 s^{-1}. These differences are attributable to detection efficiencies and non-ideal optical components in the different paths through the setup and are discussed in more detail below.

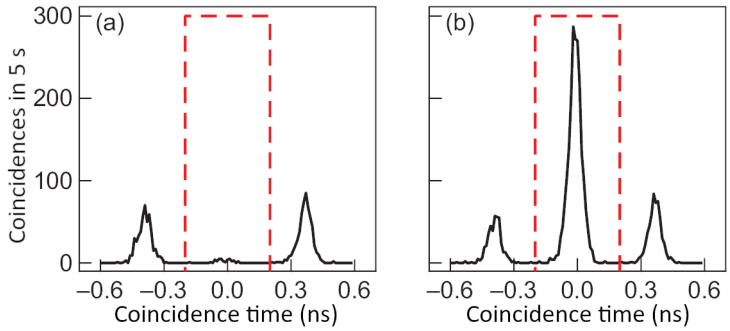

Fig. 3. Example coincidence data for a_1, b_1 coincidences taken over 5 s. The red dashed box depicts the 400 ps window around the ss and $\ell\ell$ coincidence peak. a) $\Delta\phi = 0$ and b) $\Delta\phi = \pi$.

3. Results

Fitting to Eq. 1, we measure a maximum single channel visibility of $\mathcal{V} = 0.992(6)$ and an average visibility over the four coincidences of $\mathcal{V} = 0.984(3)$, without background subtraction, as shown in Fig. 4. The values in parentheses denote the statistical uncertainty of the measurement. The

average visibility exceeds the chained Bell test visibility threshold of $\mathcal{V}_5 \approx 0.9463$ needed to overcome the PSL by 12 standard deviations.

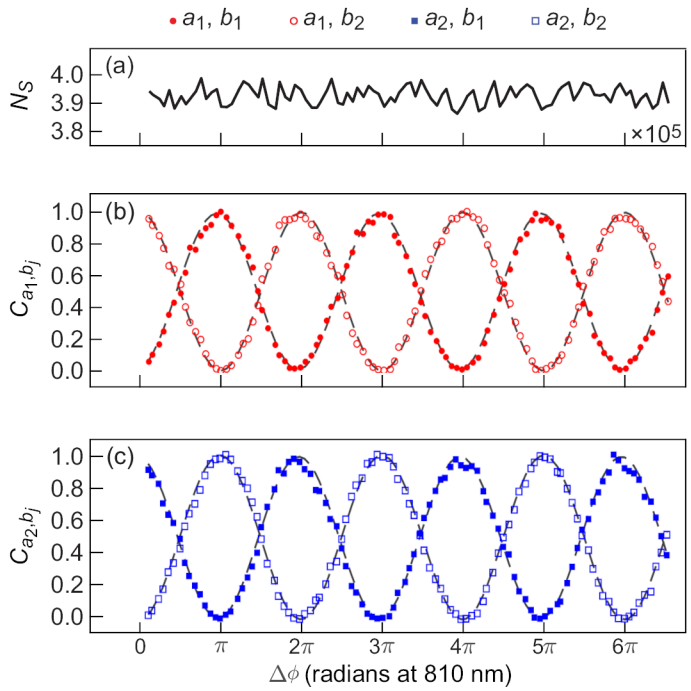

Fig. 4. Franson interferometer results. a) Total singles counts of the four detectors with an RMS of 0.8%. b) Normalized coincidence rate between detector a_1 and the detectors at Bob. c) Normalized coincidence rate between detector a_2 and the detectors at Bob. The maximum measured coincidences in the 5 s integration time for the different detector coincidences are 2055 (a_1, b_1), 3285 (a_1, b_2), 2265 (a_2, b_1), and 3585 (a_2, b_2). The gray lines in b) and c) are the fits to Eqn. 1 from which the visibilities are extracted.

In characterizing the interferometer's performance, we measure a slow drift in $\Delta\phi$ on the order 1/6$^{\text{th}}$ fringe per hour when the Franson interferometer is placed within a foam insulation enclosure on a vibration isolating optical table. The temperature of the Franson interferometer breadboard is monitored but not actively stabilized. We found that the enclosure was key in enabling high visibilities as it effectively decoupled the interferometers from external temperature variations and air currents over the ~10 minute timescale of the measurements and removed the need for any active feedback on the path lengths of the interferometers at present. A further small reduction in the maximal visibility of the SPDC source likely remains due to insufficient spectral filtering of unwanted down-conversion processes and additional fluorescence within the source and various optical fibers, as visibility increased 7% when a 1.8 nm bandpass filter is used in the 1550 nm beam path in lieu of a 12 nm bandpass filter. Spectral filtering leads to a trade-off between coincidence rate and performance; exploration of optimal spectral filtering for the source presented here is an ongoing effort [54]. Additionally, a 4 dB neutral density filter is used in the short path of Alice to equalize ss and $\ell\ell$ coincidence rates. The remaining difference in ss and $\ell\ell$ coincidence rates reduces the visibility by less than 0.6% on average [22].

4. Discussion

The high visibility demonstrated here shows both that non-degenerate biphoton sources can be used in time-energy entanglement distribution and QKD systems and that the quantum metrologies to characterize such sources are realizable. Furthermore, as waveguide SPDC sources are highly engineerable, with a wide freedom in choice of pump and emitted photon wavelengths, from degenerate to highly non-degenerate, they are well-positioned as potential interconnects between quantum networks of differing architectures. A compelling use case may be between free space quantum networks, which may operate at shorter wavelengths nearer – or in – the visible spectrum, and fiber-based quantum networks, which can take advantage of 1550 nm classical telecommunication technologies and infrastructure. A further benefit of such highly non-degenerate biphoton pairs is the degree to which the photons can be isolated from each other — as well as any residual pump light — using readily available and affordable optical components.

As in any Bell test, measurement loopholes can lead to misinterpretation of the data if not properly considered. Loopholes in a time-energy Bell test consist of those within the locality and efficiency classes that are common to all Bell tests [42, 55, 56], with the latter including the previously discussed PSL [39, 42, 43]. Fortunately, for QKD applications, it is generally more important to verify the degree of non-classical correlations than it is to close fully the Bell test loopholes [57], potentially easing some of these onerous requirements. While this experiment achieves the highest known visibility that the authors are aware of for a highly non-degenerate biphoton source [13–16, 18, 26, 32] — the highest being 90% between 606 nm and 1436 nm photons [15] — and reached a comparable visibility to a recent demonstration of up to 99.4% visibility with a ∼20 nm non-degeneracy [19].

While the measured visibility reaches the threshold for closing the PSL [39], future steps must be taken to fully close the PSL and remaining loopholes. This may be accomplished through enforcement of local post selection, a higher end-to-end efficiency from the source through the interferometers to detection, and faster and randomized choice of phase settings. Maintaining the performance achieved here with these additional constraints will require further modifications and improvements over the interferometer described above. Stabilization of the optical path lengths [50, 58], in particular, may well become necessary to maintain high visibility with increased path lengths or if deploying the interferometer in a less controlled environment. Finally, photonic integrated circuits (PICs) may also find use, where their small footprint and potential for scaling can offer advantages over a bulk optical approach. For example, a degenerate hugging Franson interferometer layout has recently been demonstrated in a silicon nitride PIC [59]. The continued development of these, and other, quantum metrologies is important in enabling the usage of highly non-degenerate sources.

5. Conclusion

Here we have described a source of highly non-degenerate correlated photons and a quantum metrology needed in verifying its suitability for quantum networking applications. Specifically, we used a Franson interferometer to characterize a waveguide SPDC source emitting a pair of correlated photons at 810 nm and 1550 nm, measuring a visibility as high as $\mathcal{V} = 0.992(6)$ for a single channel and $\mathcal{V} = 0.984(3)$ averaged over the four output channels. We have therefore shown that it is possible to realize sufficient visibilities in highly non-degenerate sources to overcome an aspect of a key Bell test loophole and be applicable to QKD networks.

Acknowledgments. Adam Fallon's research was supported by an appointment to the NASA Postdoctoral Program at the NASA Glenn Research center, administered by Oak Ridge Associated Universities under contract with NASA. The authors would like to thank the NASA Space Communications and Navigation program and the NASA Glenn Research Center's Communications and Intelligent Systems Division. We

would also like to thank the following collaborators whose work and discussions helped with this research effort: Brian Vyhnalek (NASA GRC), Yousef Chahine (NASA GRC), Bertram Floyd (HX5, LLC), Thomas Gerrits (NIST), and Alan Migdall (NIST).

Disclosures. The authors declare no conflicts of interest.

Data Availability Statement. Data underlying the results presented in this paper are not publicly available at this time but may be obtained from the authors upon reasonable request.

References

1. A. F. Barghouty, B. N. Saif, J. D. Lekki, *et al.*, "Workshop on space quantum communications and networks," Tech. rep., National Aeronautics and Space Administration (2020).
2. J. D. Wilson, D. W. Chaffee, N. C. Wilson, *et al.*, "Free-space quantum key distribution with a high generation rate potassium titanyl phosphate waveguide photon-pair source," in *Quantum Communications and Quantum Imaging XIV,* vol. 9980 (SPIE, 2016, pp. 99800U).
3. L. de Forges de Parny, O. Alibart, J. Debaud, *et al.*, "Satellite-based quantum information networks: use cases, architecture, and roadmap," Commun. Phys. **6**, 12 (2023).
4. J.-L. Liu, X.-Y. Luo, Y. Yu, *et al.*, "Creation of memory–memory entanglement in a metropolitan quantum network," Nature **629**, 579–585 (2024).
5. C. Knaut, A. Suleymanzade, Y.-C. Wei, *et al.*, "Entanglement of nanophotonic quantum memory nodes in a telecom network," Nature **629**, 573–578 (2024).
6. V. Martin, J. P. Brito, C. Escribano, *et al.*, "Quantum technologies in the telecommunications industry," EPJ Quantum Technol. **8**, 19 (2021).
7. J. Yin, Y. Cao, Y.-H. Li, *et al.*, "Satellite-based entanglement distribution over 1200 kilometers," Science **356**, 1140–1144 (2017).
8. A. Khmelev, A. Duplinsky, R. Bakhshaliev, *et al.*, "Eurasian-scale experimental satellite-based quantum key distribution with detector efficiency mismatch analysis," Opt. Express **32**, 11964–11978 (2024).
9. D. Giggenbach and A. Shrestha, "Atmospheric absorption and scattering impact on optical satellite-ground links," Int. J. Satell. Commun. Netw. **40**, 157–176 (2022).
10. H. Kaushal and G. Kaddoum, "Optical communication in space: Challenges and mitigation techniques," IEEE Commun. Surv. & Tutorials **19**, 57–96 (2017).
11. M. T. Gruneisen, M. L. Eickhoff, S. C. Newey, *et al.*, "Adaptive-optics-enabled quantum communication: A technique for daytime space-to-earth links," Phys. Rev. Appl. **16**, 014067 (2021).
12. L.-M. Duan, M. D. Lukin, J. I. Cirac, and P. Zoller, "Long-distance quantum communication with atomic ensembles and linear optics," Nature **414**, 413–418 (2001).
13. L. Ma, O. Slattery, T. Chang, and X. Tang, "Non-degenerated sequential time-bin entanglement generation using periodically poled ktp waveguide," Opt. Express **17**, 15799–15807 (2009).
14. D. Rieländer, A. Lenhard, O. J. Farìas, *et al.*, "Frequency-bin entanglement of ultra-narrow band non-degenerate photon pairs," Quantum Sci. Technol. **3**, 014007 (2017).
15. J. V. Rakonjac, D. Lago-Rivera, A. Seri, *et al.*, "Entanglement between a telecom photon and an on-demand multimode solid-state quantum memory," Phys. Rev. Lett. **127**, 210502 (2021).
16. D. Lago-Rivera, J. V. Rakonjac, S. Grandi, and H. d. Riedmatten, "Long distance multiplexed quantum teleportation from a telecom photon to a solid-state qubit," Nat. Commun. **14**, 1889 (2023).
17. M.-H. Jiang, W. Xue, Q. He, *et al.*, "Quantum storage of entangled photons at telecom wavelengths in a crystal," Nat. Commun. **14**, 6995 (2023).
18. M. Hojo, S. Tani, Y. Kobayashi, and K. Tanaka, "Coincidence measurements of two quantum-correlated photon pairs widely separated in the frequency domain," Sci. Reports **13**, 8520 (2023).
19. A. Mueller, S. I. Davis, B. Korzh, *et al.*, "High-rate multiplexed entanglement source based on time-bin qubits for advanced quantum networks," Opt. Quantum **2**, 64–71 (2024).
20. Y. Li, Y. Huang, T. Xiang, *et al.*, "Multiuser time-energy entanglement swapping based on dense wavelength division multiplexed and sum-frequency generation," Phys. Rev. Lett. **123**, 250505 (2019).
21. J. D. Franson, "Bell inequality for position and time," Phys. Rev. Lett. **62**, 2205–2208 (1989).
22. P. G. Kwiat, A. M. Steinberg, and R. Y. Chiao, "High-visibility interference in a bell-inequality experiment for energy and time," Phys. Rev. A **47**, R2472–R2475 (1993).
23. G. Lima, G. Vallone, A. Chiuri, *et al.*, "Experimental bell-inequality violation without the postselection loophole," Phys. Rev. A **81**, 040101 (2010).

24. M. Peiris, K. Konthasinghe, and A. Muller, "Franson interference generated by a two-level system," Phys. Rev. Lett. **118**, 030501 (2017).
25. J. A. Jaramillo-Villegas, P. Imany, O. D. Odele, *et al.*, "Persistent energy-time entanglement covering multiple resonances of an on-chip biphoton frequency comb," Optica **4**, 655–658 (2017).
26. X. Lu, Q. Li, D. A. Westly, *et al.*, "Chip-integrated visible–telecom entangled photon pair source for quantum communication," Nat. Phys. **15**, 373–381 (2019).
27. K.-C. Chang, X. Cheng, M. C. Sarihan, *et al.*, "648 hilbert-space dimensionality in a biphoton frequency comb: entanglement of formation and schmidt mode decomposition," npj Quantum Inf. **7**, 48 (2021).
28. K.-C. Chang, X. Cheng, M. C. Sarihan, and C. W. Wong, "Towards optimum franson interference recurrence in mode-locked singly-filtered biphoton frequency combs," Photon. Res. **11**, 1175–1184 (2023).
29. L. Achatz, L. Bulla, S. Ecker, *et al.*, "Simultaneous transmission of hyper-entanglement in three degrees of freedom through a multicore fiber," npj Quantum Inf. **9**, 45 (2023).
30. T. Zhong, F. N. C. Wong, A. Restelli, and J. C. Bienfang, "Efficient single-spatial-mode periodically-poled ktiopo4 waveguide source for high-dimensional entanglement-based quantum key distribution," Opt. Express **20**, 26868–26877 (2012).
31. T. Zhong, H. Zhou, R. D. Horansky, *et al.*, "Photon-efficient quantum key distribution using time–energy entanglement with high-dimensional encoding," New J. Phys. **17**, 022002 (2015).
32. I. Marcikic, H. de Riedmatten, W. Tittel, *et al.*, "Time-bin entangled qubits for quantum communication created by femtosecond pulses," Phys. Rev. A **66**, 062308 (2002).
33. K. Hwang, J. Seong, K. Park, *et al.*, "Entanglement witness measurement of time-bin two-qubit states using fiber-based franson interferometers," Front. Phys. **11**, 1254044 (2023).
34. J. D. Franson, "Nonlocal cancellation of dispersion," Phys. Rev. A **45**, 3126–3132 (1992).
35. J. Mower, Z. Zhang, P. Desjardins, *et al.*, "High-dimensional quantum key distribution using dispersive optics," Phys. Rev. A **87**, 062322 (2013).
36. C. Lee, Z. Zhang, G. R. Steinbrecher, *et al.*, "Entanglement-based quantum communication secured by nonlocal dispersion cancellation," Phys. Rev. A **90**, 062331 (2014).
37. K.-C. Chang, M. C. Sarihan, X. Cheng, *et al.*, "Large-alphabet time-bin quantum key distribution and einstein–podolsky–rosen steering via dispersive optics," Quantum Sci. Technol. **9**, 015018 (2023).
38. S. Fasel, N. Gisin, G. Ribordy, and H. Zbinden, "Quantum key distribution over 30 km of standard fiber using energy-time entangled photon pairs: a comparison of two chromatic dispersion reduction methods," The Eur. Phys. J. D - At. Mol. Opt. Plasma Phys. **30**, 143–148 (2004).
39. J. Jogenfors and J.-Å. Larsson, "Energy-time entanglement, elements of reality, and local realism," J. Phys. A Math. Theor. **47**, 424032 (2014).
40. T. Brougham, S. M. Barnett, K. T. McCusker, *et al.*, "Security of high-dimensional quantum key distribution protocols using franson interferometers," J. Phys. B: At. Mol. Opt. Phys. **46**, 104010 (2013).
41. T. J. Steiner, M. Shen, J. E. Castro, *et al.*, "Continuous entanglement distribution from an algaas-on-insulator microcomb for quantum communications," Opt. Quantum **1**, 55–62 (2023).
42. J. Åke Larsson, "Loopholes in bell inequality tests of local realism," J. Phys. A: Math. Theor. **47**, 424003 (2014).
43. S. Aerts, P. Kwiat, J.-A. Larsson, and M. Z˙ukowski, "Two-photon franson-type experiments and local realism," Phys. Rev. Lett. **83**, 2872–2875 (1999).
44. J. Jogenfors, A. M. Elhassan, J. Ahrens, *et al.*, "Hacking the bell test using classical light in energy-time entanglement–based quantum key distribution," Sci. Adv. **1**, e1500793 (2015).
45. D. V. Strekalov, T. B. Pittman, A. V. Sergienko, *et al.*, "Postselection-free energy-time entanglement," Phys. Rev. A **54**, R1–R4 (1996).
46. F. Vedovato, C. Agnesi, M. Tomasin, *et al.*, "Postselection-loophole-free bell violation with genuine time-bin entanglement," Phys. Rev. Lett. **121**, 190401 (2018).
47. W. Tittel, J. Brendel, N. Gisin, and H. Zbinden, "Long-distance bell-type tests using energy-time entangled photons," Phys. Rev. A **59**, 4150–4163 (1999).
48. A. Cabello, A. Rossi, G. Vallone, *et al.*, "Proposed bell experiment with genuine energy-time entanglement," Phys. Rev. Lett. **102**, 040401 (2009).
49. S. L. Braunstein and C. M. Caves, "Wringing out better bell inequalities," Ann. Phys. **202**, 22–56 (1990).
50. M. Tomasin, E. Mantoan, J. Jogenfors, *et al.*, "High-visibility time-bin entanglement for testing chained bell inequalities," Phys. Rev. A **95**, 032107 (2017).
51. J. F. Clauser, M. A. Horne, A. Shimony, and R. A. Holt, "Proposed experiment to test local hidden variable theories." Phys. Rev. Lett. **24**, 549–549 (1970).
52. AdvR, Inc., "Polarization entangled photon pair source for spacebased quantum communication," NASA SBIR contract number: 80NSSC18C0030 (2021).
53. D. N. Klyshko, "Use of two-photon light for absolute calibration of photoelectric detectors," Sov. J. Quantum Electron. **10**, 1112 (1980).
54. A. J. Fallon, D. R. Hart, E. J. Katz, *et al.*, "Dual fiber spectrometer for highly non-degenerate entanglement source," in *Proc. SPIE 12446, Quantum Computing, Communication, and Simulation III,* (SPIE, 2023, pp. 124460X).
55. J.-A. Larsson, "Bell's inequality and detector inefficiency," Phys. Rev. A **57**, 3304–3308 (1998).
56. O. Freire, *The Oxford Handbook of the History of Quantum Interpretations* (Oxford University, 2022).

57. D. J. Lum, M. D. Mazurek, A. Mikhaylov, *et al.*, "Witnessing the survival of time-energy entanglement through biological tissue and scattering media," Biomed. Opt. Express **12**, 3658–3670 (2021).
58. A. Martin, T. Guerreiro, A. Tiranov, *et al.*, "Quantifying photonic high-dimensional entanglement," Phys. Rev. Lett. **118**, 110501 (2017).
59. F. B. L. Santagiustina, C. Agnesi, A. Alarcón, *et al.*, "Experimental post-selection loophole-free time-bin and energy-time nonlocality with integrated photonics," Optica **11**, 498–511 (2024).